Nanoscale Advances

ROYAL SOCIETY OF CHEMISTRY

PAPER

View Article Online
View Journal | View Issue

Cite this: *Nanoscale Adv.*, 2023, **5**, 6514

Solution processable Si/Ge heterostructure NWs enabling anode mass reduction for practical full-cell Li-ion batteries†

Temilade Esther Adegoke,‡[a] Syed Abdul Ahad,‡[a] Ursel Bangert,[b] Hugh Geaney*[a] and Kevin M. Ryan*[a]

Here, we report the solution phase synthesis of axial heterostructure Si and Ge (hSG) nanowires (NWs). The NWs were grown in a high boiling point solvent from a low-cost Sn powder to achieve a powder form product which represents an attractive route from lab-scale to commercial application. Slurry processed anodes of the NWs were investigated in half-cell (*versus* Li-foil) and full-cell (*versus* NMC811) configurations of a lithium ion battery (LIB). The hSG NW anodes yielded capacities of 1040 mA h g^{-1} after 150 cycles which corresponds to a 2.8 times increase compared to a standard graphite (372 mA h g^{-1}) anode. Given the impressive specific and areal capacities of the hSG anodes, a full-cell test against a high areal capacity NMC811 cathode was examined. In full-cell configuration, use of the hSG anode resulted in a massive anode mass reduction of 50.7% compared to a standard graphite anode. The structural evolution of the hSG NW anodes into an alloyed SiGe porous mesh network was also investigated using STEM, EDX and Raman spectroscopy as a function of cycle number to fully elucidate the lithiation/delithiation mechanism of the promising anode material.

Received 15th August 2023
Accepted 27th August 2023

DOI: 10.1039/d3na00648d

rsc.li/nanoscale-advances

1. Introduction

Graphite with its low theoretical capacity of 372 mA h g^{-1} in Li-ion battery (LIB) anodes is unable to keep pace with the increasing energy density targets of long-range electric vehicles (EVs).[1,2] Increasing the energy density of future LIBs, requires the use of high-capacity electrode materials such as Li alloying anode materials. This requirement makes Si and Ge attractive anode materials due to the Li-rich binary alloys formed during charging resulting in their high theoretical specific capacities of 3579 mA h g^{-1} and 1384 mA h g^{-1} respectively.[3–11] However, for bulk Si and Ge, continuous cycling and Li alloy formation unfortunately causes a large volume change (~300%) that leads to pulverization and loss of electrical conductivity.[12,13] These limitations result in capacity fade and shorten the battery cycle life ultimately warranting alternative solutions.

Nanostructured morphologies such as Li-alloying anode NWs serve as promising alternatives due to their mechanically robust structure and high resistance to volume change related degradation.[9,11] NW anode offer numerous advantages including enhanced electrical conductivity, high surface area and shortened paths for Li-ion transport.[9,14] In addition, the restructuring of alloying NWs (*i.e.* Si, Ge, and Sn) into a porous network of the starting materials due to repeated Li cycling has been observed to promote capacity retention of the electrode.[11,15–17] While the majority of research have either focused on pure Si or Ge NW anodes, some reports have demonstrated the benefits of combining Si/Ge within the same NW architecture to curb the poor rate capability due to low conductivity of Si and high material cost of Ge.[18–20] The lower cost and high capacity of Si *vs.* the high conductivity (10 000×) and Li ion diffusivity (400×) of Ge is leveraged in this work to form electrodes with excellent charge storage capacity and cycling stability, likely coupled with increased mechanical strength of the Si/Ge matrix formed during cycling.[16,17,21,22] To date, a range of Si/Ge NW architectures have been formed, including alloyed NWs,[22,23] core/shell,[24] axial heterostructures[21,25] and branched structures.[17]

Si and Ge NWs architectures can be obtained *via* a variety of synthetic protocols.[26–31] A well-known route for substrate grown NWs is chemical vapour deposition (CVD). However, the low achievable yields is a significant hurdle for the use of NWs as active materials in practical applications. Alternative methods to improve NW yield include the use of high surface area substrates such as porous Ni and Cu foam.[32,33] More recently explored is the use of Cu-silicide NW networks as growth substrates for high-density NWs.[34,35] Integrating this substrates grown NW into traditional battery configurations is still

[a]*Department of Chemical Sciences and Bernal Institute, University of Limerick, Limerick, V94 T9PX, Ireland. E-mail: kevin.m.ryan@ul.ie; hugh.geaney@ul.ie*

[b]*Department of Physics and Bernal Institute, University of Limerick, Limerick, V94 T9PX, Ireland*

† Electronic supplementary information (ESI) available. See DOI: https://doi.org/10.1039/d3na00648d

‡ These authors contributed equally to the work.

challenging, especially since the inactive nanostructured network adds dead mass to the final device.

Solution based growth can ease the practical implementation of NWs since the active materials are dried to form powder products that can be slurry processed. To this end, Heitsch *et al.* demonstrated the solution–liquid–solid (SLS) synthesis of Au and Bi seeded Si NWs by thermal decomposition of trisilane in high boiling point solvent at atmospheric pressure.[36] Au has been widely employed as catalyst material for Si and Ge NWs due to its Au/Si and Au/Ge eutectic behaviour.[37] However, there has been a shift from the use of Au as catalyst for NW growth due to its high cost and low abundance. Furthermore, Au is an electrochemically inactive material in LIB anodes and adds extra mass to the final electrodes.[38] An attractive alternative catalyst is tin (Sn), which actively participates in Li cycling (with a specific capacity of 994 mA h g^{-1}) and contributes to the overall specific capacity.[6] Solution based syntheses have been used to produce Si[6,40] and Ge[5,39] NWs for slurry processed anodes. However, to the best of our knowledge, no reports have shown the formation of complex heterostructure Si and Ge (hSG) NWs for high mass loading, slurry processed anodes.

Here we demonstrate the solution phase synthesis of heterostructure Si and Ge (hSG) NWs, from Sn catalysts within a high boiling point solvent (HBS) system.[17,25,39] The Sn seeded hSG NWs were then utilized as the active material for slurry processed LIB anodes and provided synergistic advantages of both Si and Ge for Li storage. The resulting electrochemical half-cell cycling delivered a high specific capacity of 1040 mA h g^{-1} (1.5 mA h cm^{-2}) with a coulombic efficiency (C.E) of 98.9%. This capacity corresponds to 2.8 times capacity improvement in comparison to a standard graphite anode (372 mA h g^{-1}). Qualitative post-mortem STEM and EDX analysis revealed the formation of a porous and electrochemically active network that formed during repeated cycling. The hSG anode was paired with a NMC811 cathode, delivering a specific capacity of 100 mA h g^{-1} with a C.E of 99.1% at 0.2C after 100 cycles. This performance was achieved with pure hSG NWs without the use of any conductive coatings on the NWs, indicating the potential of the hSG NWs as a highly promising anode material for next-generation LIBs.

2. Materials and methods

2.1 Synthesis of hSG NWs

Sn nanoparticles (NPs) with <150 nm diameters were used as the growth catalyst for the heterostructured NWs, grown *via* SLS mechanism. Prior to the NW growth, 5 mg of Sn NPs were sonicated for 5 min in a vial containing 9 mL of squalane (99% Aldrich). The Sn Np/squalane solution was added into the long-neck Pyrex, round bottomed flask and connected to a condenser sealed with a septum cap. The reaction flask was setup inside a three-zone furnace and connected to a Schlenk line for control of chemical reactivity during synthesis. Using the Schlenk line to eliminate all residual moisture, the furnace was heated to 125 °C under vacuum (<300 mTorr) for 30 min and then switched to Ar gas. The solution was then heated to the required reaction temperatures under a continuous Ar flow and reflux through a water condenser. The reaction temperature varied from 430 °C to 460 °C to facilitate the decomposition of the precursors.

Si NW segment. The growth of Si NWs was carried out at reaction temperature 460 °C. First, 1 mL of phenylsilane (PS) was injected through the septum cap into the reaction flask. After 5 min, 0.02 mL of a $LiBH_4$ solution was also injected to reduce the surface oxides on the Sn catalysts and enhance Si NW growth. The reaction was allowed to proceed for a duration of 40 min.

Ge NW segment. The reaction temperature was lowered to 430 °C and allowed to stabilize over a 15 min duration. The Ge precursor was prepared by mixing triphenylgermane (TPG) and squalane in a 1 : 4 ratio and sonicated for 30 min. Subsequently, 0.5 mL of the mixture was injected into the reaction system and the reaction was allowed to proceed for 8 min. The reaction was quenched by turning off the furnace and allowed to cool to room temperature before the flask was removed from the furnace.

Washing steps. The flask was sonicated for 5 s to redisperse the NWs from the walls of the flask into the residual squalane solution at the bottom of the flask. Followed by centrifuging the NW solution at 5000 rpm for 10 min. The supernatant was discarded and redispersed in a toluene/isopropanol (1 : 1) mixture and repurified by centrifugation. This washing step was repeated two more times and the precipitate was collected and dried in a vacuum oven at 100 °C for 12 h, resulting in a NW yield of 11 mg.

2.2 Material characterisation

The hSG NWs were disseminated in ethanol. The solution was drop cast onto a 1 cm × 1 cm copper foil and lacey carbon sheet (Cu grid) for electron microscopy characterisation. Scanning electron microscopy (SEM) and scanning transmission electron microscopy (STEM) data were obtained. An FEI (Thermo) Helios G4 CX Dual-beam microscope with an Oxford X-maxN 50 Energy dispersive X-ray spectroscopy (EDX) detector was used for all SEM analyses of the NWs on copper foil. The operating parameters were 20 kV & 1.4 nA. The Cu TEM grid anchoring the NWs was placed in an FEI double-tilt holder, and STEM measurements were carried out in the Thermo-Fisher Scientific FEI double-aberration-corrected monochromated Titan Themis S/TEM. Images were recorded with the high-angle annular dark-field (HAADF) detectors for *Z*-contrast imaging to highlight the transition between the Ge and Si segments of the NWs.

Additionally, EDX maps were captured in HAADF STEM mode. X-ray diffraction (XRD) analysis of hSG NWs was performed using a zero-background disk. The XRD instrument was a PANalytical Empyrean instrument fitted with a Cu K_α source (λ = 1.5418 Å) and an X'celerator detector. Raman spectroscopy measurements were performed with a Horiba Labram 300 spectrometer instrument fitted with a 532 nm laser.

2.3 Electrochemical measurements

A hSG NW slurry mixture of 60% hSG, 20% carbon black and 20% carboxymethyl cellulose (CMC) binder and DI water was

casted on a copper (Cu, 16–18 μm) foil. The slurry was finally dried overnight in a vacuum oven at 100 °C. The hSG NW electrodes were cut in circular shape with an average mass loading of 1.3–1.5 mg cm^{-2}. For electrochemical characterization two electrodes CR2032 coin cells or Swagelok cells were assembled in an Argon filled glove box with O_2 and moisture levels kept below 1 ppm. A Celgard 2325 membrane was used as electrode separator and an electrolyte solution of 1 M $LiPF_6$ in ethylene carbonate/diethyl carbonate (1 : 1 v/v) mixed with 10% fluoroethylene carbonate. An electrolyte volume of 80 μL was used for both half and full-cell studies.

For theoretical capacity calculation of hSG electrode, the mass of all active materials *i.e.* Si, Ge and Sn was considered while (Si) 3579 mA h g^{-1}, (Ge) 1384 mA h g^{-1} and (Sn) 994 mA h g^{-1} were used as theoretical capacities (Fig. S1†). The theoretical capacity of hSG was calculated to be 2411 mA h g^{-1}. Half-cell testing was conducted by pairing the hSG NW electrodes with Li foil as the counter/reference electrode and cycled within a potential range of 0.011–2.0 *versus* Li/Li+. The half-cell was tested at 0.1C (5 cycles) and eventually at 0.2C for long-term cycling. For full cell assembly, NMC811 (9.71 mg cm^{-2}, 2 mA h cm^{-2}) tape procured from NEI corporation was used directly as cathode and a P/N ratio of 1.18 was used to assemble hSG NW–NMC full-cell. For full cell testing, hSG anode was cycled for 5 cycles and stopped at 50% prelithiation stage before pairing it with a NMC811 cathode. The full cell was cycled at 0.1C (5 cycles) and eventually at 0.2C between 2.8–4.2 V. All electrochemical testing and electrochemical impedance spectroscopy was conducted using Biologic Instruments at ambient laboratory temperatures.

3. Results and discussion

Fig. 1a illustrates the solution–liquid–solid (SLS) synthetic approach for the growth of hSG NWs. This solution-based synthetic route consists of a high boiling point solvent (HBS) and Sn nanoparticles that form a eutectic with the Si and Ge reactants.[21,25,39–41] Si and Ge segments of the NWs were synthesized by sequential thermal decomposition of PS and TPG in HBS squalane at temperatures greater than 400 °C leading to a yield of hSG NWs (>10 mg per synthesis). This achievable yield is 10-folds higher than what is currently been obtained for hSG NWs grown on low surface area planar substrates.[16,17,21] XRD analysis in Fig. 1b further confirmed the successful synthesis of crystalline Si and Ge in hSG NWs with peaks corresponding to tetragonal Sn, cubic Si and cubic Ge. A scanning electron microscopy (SEM) image of the SLS grown hSG NWs is shown in Fig. 1c. The high degree of polydispersity in the NW diameter can be associated with the varied size distribution of the Sn NP used as catalyst. A further contributor may be the low melting point of Sn, resulting in nanoparticle agglomeration from the high reactivity and chemical instability of Sn at high temperatures.[42] The NWs are typically several microns long and the product contains a mixture of straight and bent NWs. The average diameter of the Si and Ge segments were 180 nm and 228 nm respectively and the corresponding size distribution is shown in Fig. S2.† The Sn : Si : Ge ratios were investigated using SEM EDX detector where the weight% of multiple areas of the substrate were determined and averaged as 18 : 50 : 32 (Fig. S1†). The Si and Ge contributions as well as NW yield increases at longer growth times making the Sn : Si : Ge ratios tunable. TEM-EDX mapping clearly show the variation in elemental composition along the NW length (Fig. 1d).

High angle annular dark field scanning transmission electron microscopy (HAADF-STEM) and EDX elemental mapping revealed the heterointerface and the distribution of Si and Ge (Fig. 2). Fig. 2a and b show low and high magnification views of the hSG NW and a diameter expansion beginning at the Ge segment of the NW. The high resolution image in Fig. 2d shows the resolved atomic columns along the NW heterointerface; the interplanar spacing (d) is 0.3236 nm for crystalline Si and 0.3428 nm for crystalline Ge. The Fast Fortier transform (FFT) viewed down the [110] zone axis confirmed the NW's ⟨111⟩ growth direction. FFTs spots in Fig. 2e were indexed with diamond cubic Si and Ge ($Fd\bar{3}m$).

Additionally, we investigated the defects characteristics of the hSG NWs (Fig. S3†). The main defects observed in the SLS grown NWs were twin boundaries (TB) and stacking faults (SF), parallel to the growth direction. The NW overview (Fig. S3†) exhibits a SF that originates in the Si segment of the NW and extend in to the Ge segment which was also previously observed for Sn seeded heterostructures.[25,43] High-magnification and atomic resolution STEM images of the hSG NW show the SF along its length in clearer detail. The SF propagated in the ⟨111⟩ direction evident by the presence of streaks in the (111) type plane, which are characteristics of planar defects.[40,44–47] Planar faults are often growth mechanism dependent and are present in high densities in Vapour Liquid Solid (VLS) grown NWs.[46] The SLS mechanism is analogous to VLS and similar defects have been observed in Si[21,48] and Ge[44,46,49] NWs. Defect probabilities in Si and Ge NWs have been seen to be influenced by the instability of the metal catalyst which in turn influences the kinetics of the NW growth including defect propagation.[25,39,45] Previous reports have demonstrated that not only can defect act as catalyst doping sites and enhance the conductivity,[25,50–52] but may also influence the mechanical properties of nanostructures, improving their plasticity and strength. This suggests that the presence of SF in the hSG NWs may contribute to strain relaxation the NWs where the origin of strain is due to lithium insertion and extraction.[53,54]

The electrochemical performance of hSG NWs was gauged by pairing with a Li counter electrode in a half-cell configuration. The galvanostatic cycling showed that hSG NWs delivered an initial lithiation capacity of 2544 mA h g^{-1} at 0.1C (Fig. 3a). After initial pre-cycling at 0.1C, the hSG NW anode delivered a lithiation capacity of 1742 mA h g^{-1} at 0.2C with a high coulombic efficiency (C.E) of 97.6%. In comparison, the Si NWs anode delivered an initial specific capacity of 1140 mA h g^{-1} at 0.2C with a C.E of 96%. After 150 cycles, the hSG NW anode further delivered a high specific capacity of 1040 mA h g^{-1} (1.5 mA h cm^{-2}) with an average C.E of 98.9% notable due to the increased cycling stability offered by Ge. In contrast, the specific capacity of the Si NWs anode decreased significantly to 610 mA h g^{-1} after 150 cycles, which is 1.7 times lower than that

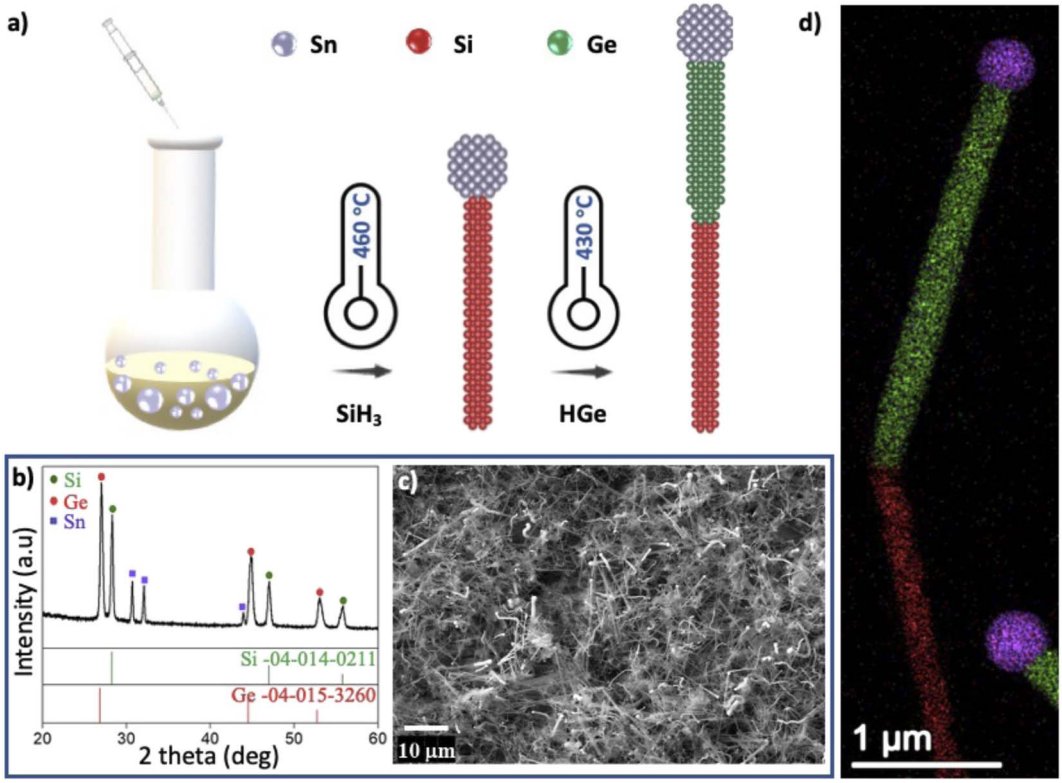

Fig. 1 (a) Schematics of the solution phase growth of Sn seeded hSG NWs, (b) corresponding XRD analysis, (c) SEM image of hSG NWs, (d) EDX elemental maps showing Sn, Si and Ge segments in a single hSG NW.

of the hSG NW anode. This suggests that the properties of both the high capacity Si segment and the high Li-ion diffusivity/conductivity Ge segment can be employed together in the form of hSG NWs to develop anodes with high cyclic performance for Li-ion batteries. The specific capacity of the hSG NW anode achieved after 150 cycles is approximately 2.8 times higher than a standard graphite anode (372 mA h g^{-1}), making the hSG anode a viable anode to achieve higher energy densities in Li-ion full cell configurations as well. It should be noted that the areal capacity of 1.5 mA cm^{-2} is significantly higher than what was achieved for hSG directly grown on planar current collectors in our previous work, where we showed areal capacities of <0.2 mA h cm^{-2}.[16]

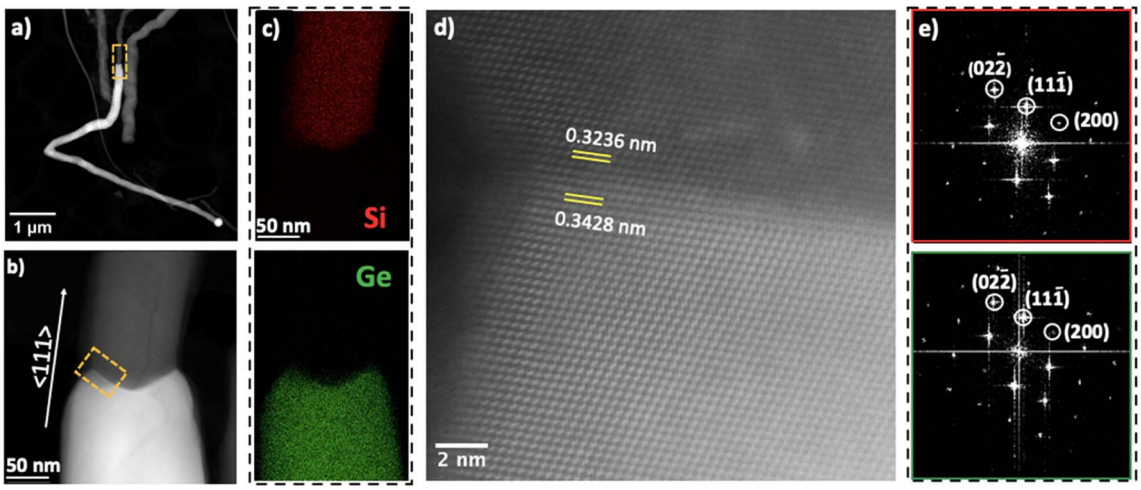

Fig. 2 HAADF-STEM analysis of hSG NW (a) low-magnification STEM image showing the overview of the NW, (b) a higher magnification STEM image, (c) EDX maps with Si in red and Ge in green, (d) an atomic-resolution HAADF-STEM taken from the same NW viewed down the [110] zone axis, indicating a coherent interface between the Si and Ge segments, (e) FFT signals corresponding to the individual Si and Ge segments of the atomic-resolution STEM image.

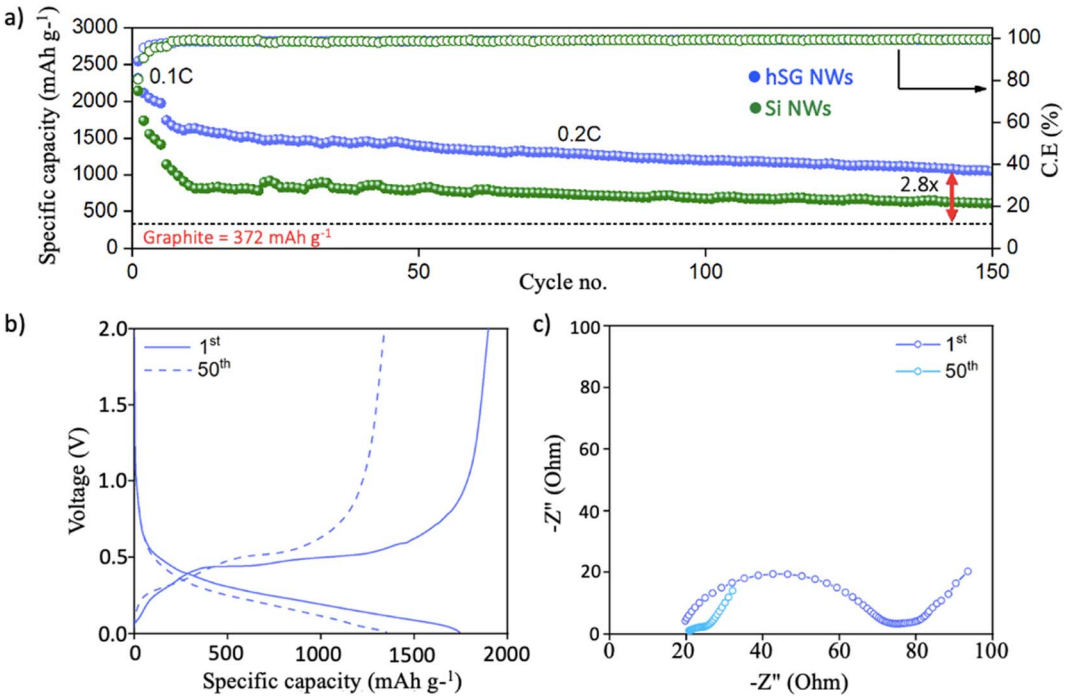

Fig. 3 (a) Cyclic performance of hSG NWs and Si NWs at 0.2C cycled between 0.011–2.0 V, (b) corresponding voltage–specific capacity plot and (c) EIS analysis of hSG NWs after 1st and 50th cycle of hSG NWs.

The voltage–specific capacity plot of hSG anode after the 1st and 50th cycle (at 0.2C) show stable lithiation/delithiation profiles during cycling (Fig. 3b). The corresponding voltage–specific capacity profile of Si NWs are given in Fig. S4† for comparison. The Electrochemical impedance spectroscopy (EIS) analysis was performed after the 1st and 50th cycle to understand the reaction kinetics during cycling (Fig. 3c). The EIS analysis shows a charge-transfer resistance (R_{ct}) of 47.9 ohm after 1st cycle which decreased to 5.1 Ohm (9 times lower) after 50th cycle (Fig. S5, Table S1†). The low R_{ct} value after 50th cycle signifies stable SEI formation, minimizing electrolyte decomposition and capacity losses during cycling.[55,56] The rate capability test performed at 0.1, 0.2, 0.5 and 1C delivered specific capacities of 2300, 1786, 1511 and 1146 mA h g^{-1} respectively (Fig. S6a†). The corresponding voltage–specific capacity plot of hSG NWs at various C-rates is given in Fig. S6b.†

The structural evolution of hSG NWs was studied using STEM analysis in combination with the electrochemical kinetics during cycling. The differential capacity (dQ/dV) plot of hSG NWs after the 5th cycle (at 0.2C) shows several peaks during the lithiation/delithiation steps (Fig. 4a). Specifically, the peak appearing during lithiation at 0.65 V (A) corresponds to lithiation of the Sn[57,58] while the peak appearing at 0.41 V (B) corresponds to lithiation of the Ge.[11] Other peaks are also observed at 0.25 V (C) and 0.08 V (D) belonging to lithiation of Si.[45,59,60] Similarly, during delithiation step, the peak at 0.43 V (E) indicate Si delithiation,[45,59] another peak at 0.51 V (F) indicates delithiation of Ge and while peaks at 0.60 V (G), 0.72 V (H) and 0.80 V (I) were attributed to delithiation of Sn.[11,45,61] The individual lithiation/delithiation peaks originating from Si, Ge and Sn show that all three materials are active during the electrochemical cycling. STEM analysis of hSG NWs after 5 cycles shows conversion of Si and Ge segments into a mesh-like structure due to the Li insertion and extraction while still maintaining the initial NW outline and the interface separating both segments. The visible STEM contrast shows a distinction between the Si and Ge segments even after 5 cycles with EDX elemental maps of all the active materials. The transformation of the Sn seed can also be seen in (Fig. S7a†) and both Si and Ge segments have also become amorphous and no longer signify an ordered crystalline structure (Fig. S7b and c†).

To further understand this structural and compositional evolution, the differential capacity plots after 25th and 50th cycles and the corresponding structural changes in hSG NWs were analysed (Fig. 4b and c). The dQ/dV plot after 25th and 50th cycle shows lithiation peaks at J (0.46 V), K (0.29 V), M (0.14 V) which corresponds to Ge lithiation and L (0.24 V), N (0.04 V) corresponds to lithiation of Si.[62–65] The major delithiation peak at 0.30 V (O) and 0.51 V (P) corresponded to the delithiation of Si and Ge respectively. The dQ/dV plots of pure Si NWs (Fig. S8†) clearly shows the absence of Ge NW lithiation/de-lithiation peaks, which confirms the combined electrochemical activity of Si and Ge in hSG anode. The merging of most of the peaks (as compared to 5th cycle) suggests that during repeated electrochemical cycling, the Si and Ge segments have alloyed.[17] Corresponding STEM analysis of the hSG anode after 25 cycles, suggests complete restructuring of the initial NW morphology into a mesh structure and Li- assisted welding of neighbouring individual NWs.[11,16] EDX elemental maps showing complete

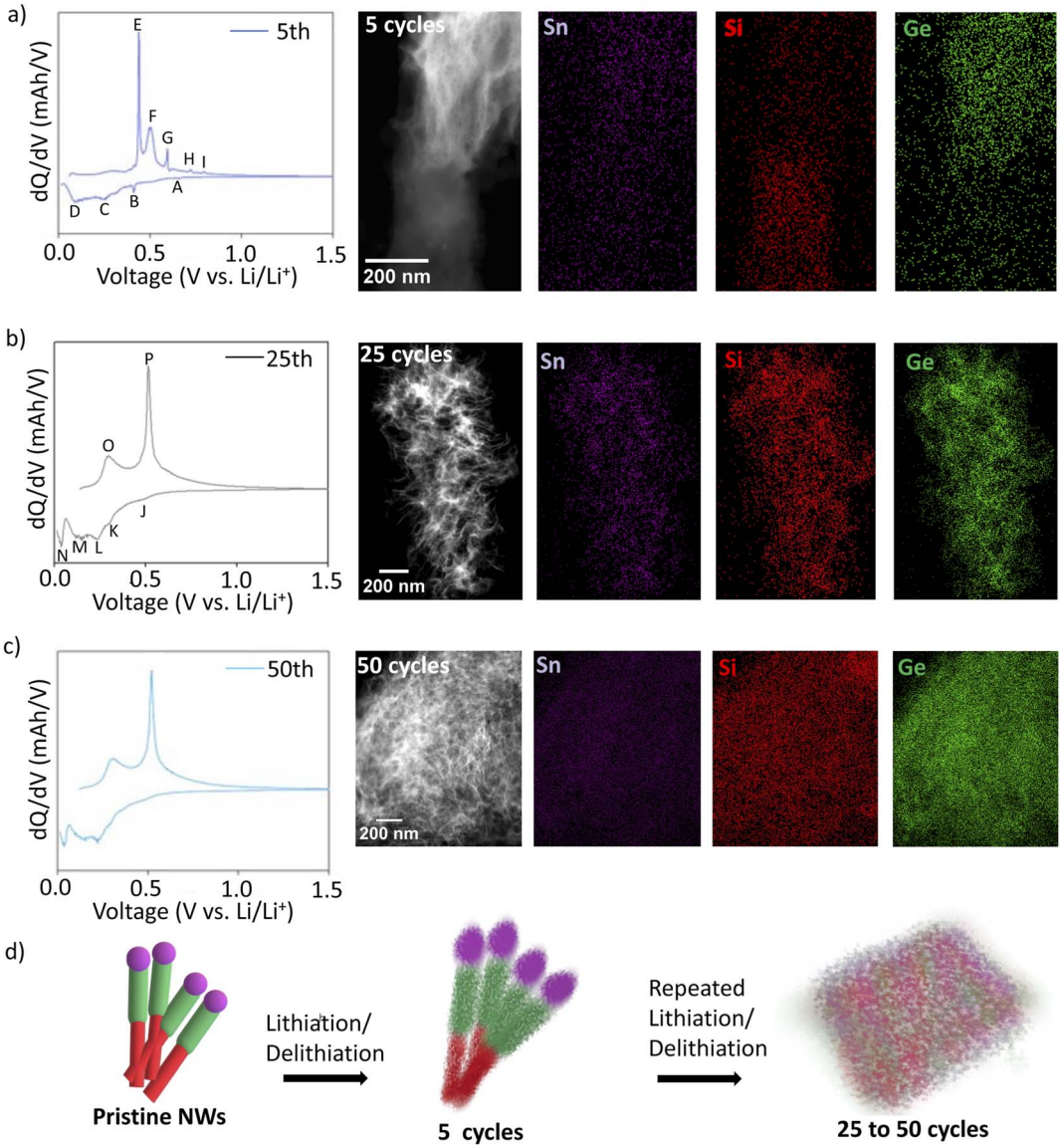

Fig. 4 Differential capacity plot of hSG NWs after (a) 5th, (b) 25th and (c) 50th cycle at 0.2C with corresponding STEM and EDX images. (d) Schematic illustration of the structural evolution of hSG NW during Li cycling.

overlap and uniform distribution of Si (red), Ge (green) and Sn purple segments (Fig. 4b).

Also, STEM analysis after 50 cycles shows agglomeration and merging of several neighbouring hSG mesh structure, creating bigger mesh interconnected networks during further cycling (Fig. 4c). Formation of such mesh-like network might be another reason for low R_{ct} value after 50 cycles, suggesting faster electrochemical kinetics as well. Moreover, the interconnected mesh structure could help with accommodating large volume expansion during the lithiation/delithiation process.[17] To confirm the presence of a Si–Ge alloy in the cycled anode, Raman spectroscopy was performed on the pristine as well as cycled anodes after the 5th and 25th cycle (Fig. S9†). The Raman spectra of the pristine hSG NWs and hSG NWs after 5 cycles, show the presence of only two peaks around 300 cm^{-1} and 500 cm^{-1}, originating from Ge–Ge and Si–Si bond respectively. However after 25 cycles, an additional peak around 400 cm^{-1} originating from Ge–Si bond appears, which confirms the presence of SiGe alloy in the cycled NWs.[17,66,67] This suggests that with increasing number of cycles, Si and Ge segments intermix to form SiGe alloy electrochemically as well. This re-affirms the evidence shown in the differential capacity plots and STEM analysis that the Si and Ge segments in hSG NWs converts to an SiGe alloy during electrochemical cycling (Fig. 4d). This feature is unique since earlier report suggest SiGe alloy NWs were synthesized *via* CVD process at higher temperatures and/or through simultaneous magnetron sputtering of Si and Ge on substrates.[22,66]

hSG NWs were also paired with high areal capacity NMC811 (2 mA h cm^{-2}) cathodes in a full-cell configuration. The galvanostatic cycling was conducted between 4.2–2.8 V at 0.2C. After initial pre-cycling at 0.1C, the hSG NW/NMC full-cell delivered a specific capacity of 161 mA h g^{-1} at 0.2C with a coulombic efficiency of 96.6% (Fig. 5a). Thereafter, the hSG/NMC cell

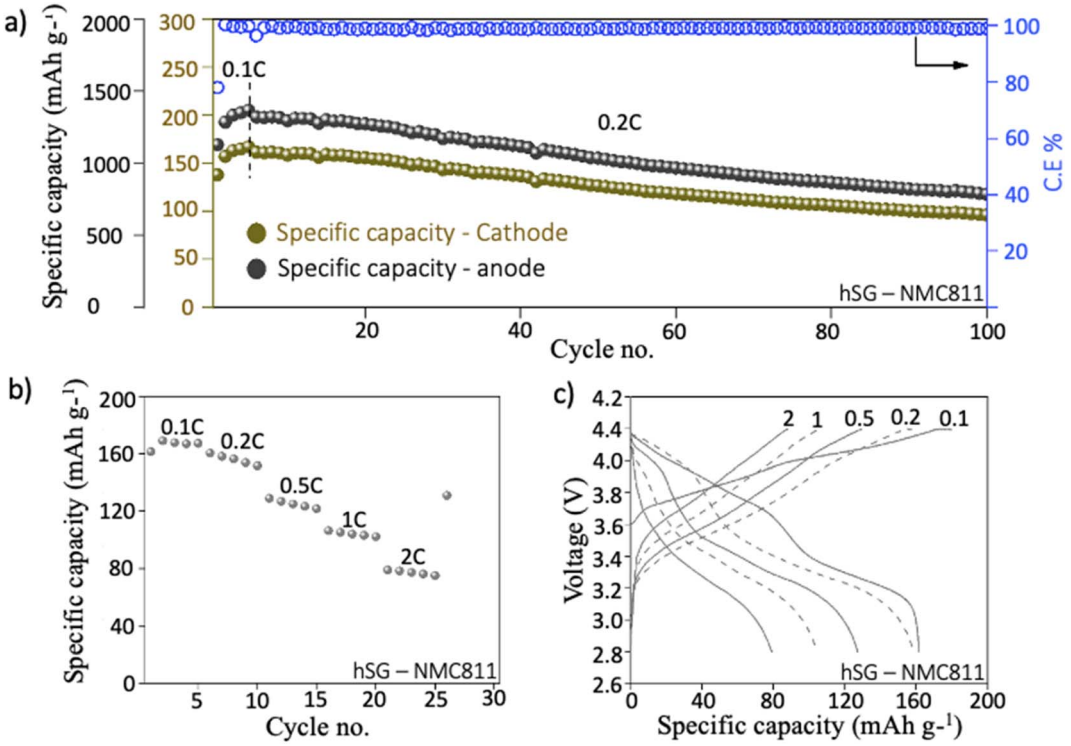

Fig. 5 (a) Cyclic performance of hSG–NMC811 at 0.2C cycled between 4.2–2.8 V, (b) rate capability analysis of hSG–NMC811 cell and (c) corresponding voltage–specific capacity graph of rate capability test at various C-rates.

demonstrated a specific capacity of 127 mA h g^{-1} after 50 cycles with a capacity retention of 79%. The capacity settled at ~100 mA h g^{-1} after 100 cycles with an average coulombic efficiency of 99.1%. The corresponding anode specific capacity is also given with the capacity fade expected due to the limited Li supply (from NMC811) cathode as compared to Li metal (half-cell). With a P/N ratio of 1.18 used in balancing hSG–NMC811 full cell, a 50.7% decrease in the total anode mass (including binder and conductive additive) was observed as compared to a standard graphite–NMC811 full cell (Table S2†). Such decrease in the anode weight is highly beneficial in terms of increasing the total energy density of commercial batteries using hSG NW anode. The corresponding voltage–specific capacity plot after 1st and 50th cycle is given in Fig. S10.† To test the electrochemical performance of hSG/NMC configuration at high C-rates, rate capability test at 0.1, 0.2, 0.5, 1 & 2C delivered a specific capacity of 162, 160, 129, 106 and 80 mA h g^{-1}, respectively (Fig. 5b). The corresponding voltage–specific capacity plots show stable lithiation/delithiation profile of full cell at various C-rates (Fig. 5c). Overall, the hSG demonstrated robust performance in both half- and full-cell configurations, emphasizing its suitability for high performance Li-ion battery anodes.

4. Conclusion

In summary, we have reported a solution-based synthesis of hSG NWs using low-cost Sn powder. Unlike NW growth on planar substrates with low masses, the solution-based synthesis technique of hSG NWs has a potential of scaling up (with product in powder form), paving the way for high mass loadings during slurry processing. The hSG NW anode delivered an excellent specific capacity of 1040 mA h g^{-1} after 150 cycles with an average coulombic efficiency of 98.9%. The detailed post-mortem characterisation revealed structural evolution of the hSG NWs with Si and Ge segments converting into a SiGe alloy over extended cycling. The conversion of the starting NW morphology into an interconnected mesh-like structure contributed towards enhanced electron-transfer kinetics. Finally, the use of hSG NW anode in Li-ion full-cells was demonstrated by pairing with high areal capacity NMC cathodes, delivering a specific capacity of 100 mA h g^{-1} after 100 cycles at 0.2C with an average C.E of 99.1%. Overall, this report validates the successful use of segmented Sn seeded Si–Ge NWs, which can replace low-capacity graphite anodes to increase energy density in future high-energy LIBs.

Conflicts of interest

There are no conflicts to declare.

References

1 B. Scrosati, Recent advances in lithium ion battery materials, *Electrochim. Acta*, 2000, **45**(15), 2461–2466.
2 M. M. Thackeray, C. Wolverton and E. D. Isaacs, Electrical energy storage for transportation—approaching the limits

of, and going beyond, lithium-ion batteries, *Energy Environ. Sci.*, 2012, **5**(7), 7854–7863.
3 J. O. Besenhard, J. Yang and M. Winter, Will advanced lithium-alloy anodes have a chance in lithium-ion batteries?, *J. Power Sources*, 1997, **68**(1), 87–90.
4 T. D. Bogart, A. M. Chockla and B. A. Korgel, High capacity lithium ion battery anodes of silicon and germanium, *Curr. Opin. Chem. Eng.*, 2013, **2**(3), 286–293.
5 A. M. Chockla, K. C. Klavetter, C. B. Mullins and B. A. Korgel, Solution-Grown Germanium Nanowire Anodes for Lithium-Ion Batteries, *ACS Appl. Mater. Interfaces*, 2012, **4**(9), 4658–4664.
6 A. M. Chockla, K. C. Klavetter, C. B. Mullins and B. A. Korgel, Tin-Seeded Silicon Nanowires for High Capacity Li-Ion Batteries, *Chem. Mater.*, 2012, **24**(19), 3738–3745.
7 Y. Yao, M. T. McDowell, I. Ryu, H. Wu, N. Liu, L. Hu, W. D. Nix and Y. Cui, Interconnected Silicon Hollow Nanospheres for Lithium-Ion Battery Anodes with Long Cycle Life, *Nano Lett.*, 2011, **11**(7), 2949–2954.
8 H. Lee, M. G. Kim, C. H. Choi, Y.-K. Sun, C. S. Yoon and J. Cho, Surface-Stabilized Amorphous Germanium Nanoparticles for Lithium-Storage Material, *J. Phys. Chem. B*, 2005, **109**(44), 20719–20723.
9 C. K. Chan, H. Peng, G. Liu, K. McIlwrath, X. F. Zhang, R. A. Huggins and Y. Cui, High-performance lithium battery anodes using silicon nanowires, *Nat. Nanotechnol.*, 2008, **3**(1), 31–35.
10 C.-M. Park, J.-H. Kim, H. Kim and H.-J. Sohn, Li-alloy based anode materials for Li secondary batteries, *Chem. Soc. Rev.*, 2010, **39**(8), 3115–3141.
11 T. Kennedy, E. Mullane, H. Geaney, M. Osiak, C. O'Dwyer and K. M. Ryan, High-Performance Germanium Nanowire-Based Lithium-Ion Battery Anodes Extending over 1000 Cycles Through *In Situ* Formation of a Continuous Porous Network, *Nano Lett.*, 2014, **14**(2), 716–723.
12 U. Kasavajjula, C. Wang and A. J. Appleby, Nano- and bulk-silicon-based insertion anodes for lithium-ion secondary cells, *J. Power Sources*, 2007, **163**(2), 1003–1039.
13 J. H. Ryu, J. W. Kim, Y.-E. Sung and S. M. Oh, Failure Modes of Silicon Powder Negative Electrode in Lithium Secondary Batteries, *Electrochem. Solid-State Lett.*, 2004, **7**(10), A306.
14 H. Wu and Y. Cui, Designing nanostructured Si anodes for high energy lithium ion batteries, *Nano Today*, 2012, **7**(5), 414–429.
15 T. Kennedy, M. Brandon, F. Laffir and K. M. Ryan, Understanding the influence of electrolyte additives on the electrochemical performance and morphology evolution of silicon nanowire based lithium-ion battery anodes, *J. Power Sources*, 2017, **359**, 601–610.
16 K. Stokes, G. Flynn, H. Geaney, G. Bree and K. M. Ryan, Axial Si–Ge Heterostructure Nanowires as Lithium-Ion Battery Anodes, *Nano Lett.*, 2018, **18**(9), 5569–5575.
17 T. Kennedy, M. Bezuidenhout, K. Palaniappan, K. Stokes, M. Brandon and K. M. Ryan, Nanowire Heterostructures Comprising Germanium Stems and Silicon Branches as High-Capacity Li-Ion Anodes with Tunable Rate Capability, *ACS Nano*, 2015, **9**(7), 7456–7465.
18 J. Li, N. J. Dudney, X. Xiao, Y. T. Cheng, C. Liang and M. W. Verbrugge, Asymmetric rate behavior of Si anodes for lithium-ion batteries: ultrafast de-lithiation *versus* sluggish lithiation at high current densities, *Adv. Energy Mater.*, 2015, **5**(6), 1401627.
19 D. Wang, Y.-L. Chang, Q. Wang, J. Cao, D. B. Farmer, R. G. Gordon and H. Dai, Surface chemistry and electrical properties of germanium nanowires, *J. Am. Chem. Soc.*, 2004, **126**(37), 11602–11611.
20 A. Esmanski and G. A. Ozin, Silicon inverse-opal-based macroporous materials as negative electrodes for lithium ion batteries, *Adv. Funct. Mater.*, 2009, **19**(12), 1999–2010.
21 S. Kilian, K. McCarthy, K. Stokes, T. E. Adegoke, M. Conroy, I. S. Amiinu, H. Geaney, T. Kennedy and K. M. Ryan, Direct Growth of Si, Ge, and Si–Ge Heterostructure Nanowires Using Electroplated Zn: An Inexpensive Seeding Technique for Li-Ion Alloying Anodes, *Small*, 2021, **17**(10), 2005443.
22 K. Stokes, H. Geaney, G. Flynn, M. Sheehan, T. Kennedy and K. M. Ryan, Direct Synthesis of Alloyed $Si_{1-x}Ge_x$ Nanowires for Performance-Tunable Lithium Ion Battery Anodes, *ACS Nano*, 2017, **11**(10), 10088–10096.
23 H. Kim, Y. Son, C. Park, M.-J. Lee, M. Hong, J. Kim, M. Lee, J. Cho and H. C. Choi, Germanium silicon alloy anode material capable of tunable overpotential by nanoscale Si segregation, *Nano Lett.*, 2015, **15**(6), 4135–4142.
24 L. J. Lauhon, M. S. Gudiksen, D. Wang and C. M. Lieber, Epitaxial core–shell and core–multishell nanowire heterostructures, *Nature*, 2002, **420**(6911), 57–61.
25 H. Geaney, E. Mullane, Q. M. Ramasse and K. M. Ryan, Atomically Abrupt Silicon–Germanium Axial Heterostructure Nanowires Synthesized in a Solvent Vapor Growth System, *Nano Lett.*, 2013, **13**(4), 1675–1680.
26 Y. Wu and P. Yang, Germanium Nanowire Growth *via* Simple Vapor Transport, *Chem. Mater.*, 2000, **12**(3), 605–607.
27 J. D. Holmes, K. P. Johnston, R. C. Doty and B. A. Korgel, Control of Thickness and Orientation of Solution-Grown Silicon Nanowires, *Science*, 2000, **287**(5457), 1471–1473.
28 L. Schubert, P. Werner, N. D. Zakharov, G. Gerth, F. M. Kolb, L. Long, U. Gösele and T. Y. Tan, Silicon nanowhiskers grown on ⟨111⟩Si substrates by molecular-beam epitaxy, *Appl. Phys. Lett.*, 2004, **84**(24), 4968–4970.
29 A. M. Morales and C. M. Lieber, A laser ablation method for the synthesis of crystalline semiconductor nanowires, *Science*, 1998, **279**(5348), 208–211.
30 M.-L. Zhang, K.-Q. Peng, X. Fan, J.-S. Jie, R.-Q. Zhang, S.-T. Lee and N.-B. Wong, Preparation of Large-Area Uniform Silicon Nanowires Arrays through Metal-Assisted Chemical Etching, *J. Phys. Chem. C*, 2008, **112**(12), 4444–4450.
31 H. Geaney, C. Dickinson, C. A. Barrett and K. M. Ryan, High density germanium nanowire growth directly from copper foil by self-induced solid seeding, *Chem. Mater.*, 2011, **23**(21), 4838–4843.
32 S. Jing, H. Jiang, Y. Hu and C. Li, Directly grown Si nanowire arrays on Cu foam with a coral-like surface for lithium-ion batteries, *Nanoscale*, 2014, **6**(23), 14441–14445.

33 Q. Zhang, H. Chen, L. Luo, B. Zhao, H. Luo, X. Han, J. Wang, C. Wang, Y. Yang and T. Zhu, Harnessing the concurrent reaction dynamics in active Si and Ge to achieve high performance lithium-ion batteries, *Energy Environ. Sci.*, 2018, **11**(3), 669–681.

34 G. A. Collins, S. Kilian, H. Geaney and K. M. Ryan, A Nanowire Nest Structure Comprising Copper Silicide and Silicon Nanowires for Lithium-Ion Battery Anodes with High Areal Loading, *Small*, 2021, **17**(34), 2102333.

35 I. S. Aminu, H. Geaney, S. Imtiaz, T. E. Adegoke, N. Kapuria, G. A. Collins and K. M. Ryan, A Copper Silicide Nanofoam Current Collector for Directly Grown Si Nanowire Networks and their Application as Lithium-Ion Anodes, *Adv. Funct. Mater.*, 2020, **30**(38), 2003278.

36 A. T. Heitsch, D. D. Fanfair, H.-Y. Tuan and B. A. Korgel, Solution–Liquid–Solid (SLS) Growth of Silicon Nanowires, *J. Am. Chem. Soc.*, 2008, **130**(16), 5436–5437.

37 X. Lu, D. D. Fanfair, K. P. Johnston and B. A. Korgel, High Yield Solution–Liquid–Solid Synthesis of Germanium Nanowires, *J. Am. Chem. Soc.*, 2005, **127**(45), 15718–15719.

38 A. M. Chockla, T. D. Bogart, C. M. Hessel, K. C. Klavetter, C. B. Mullins and B. A. Korgel, Influences of gold, binder and electrolyte on silicon nanowire performance in Li-ion batteries, *J. Phys. Chem. C*, 2012, **116**(34), 18079–18086.

39 G. Flynn, K. Stokes and K. M. Ryan, Low temperature solution synthesis of silicon, germanium and Si–Ge axial heterostructures in nanorod and nanowire form, *Chem. Commun.*, 2018, **54**(45), 5728–5731.

40 S. A. Dayeh, J. Wang, N. Li, J. Y. Huang, A. V. Gin and S. T. Picraux, Growth, Defect Formation, and Morphology Control of Germanium–Silicon Semiconductor Nanowire Heterostructures, *Nano Lett.*, 2011, **11**(10), 4200–4206.

41 C.-Y. Wen, M. C. Reuter, J. Bruley, J. Tersoff, S. Kodambaka, E. A. Stach and F. M. Ross, Formation of Compositionally Abrupt Axial Heterojunctions in Silicon-Germanium Nanowires, *Science*, 2009, **326**(5957), 1247–1250.

42 T. Hanrath and B. A. Korgel, Nucleation and Growth of Germanium Nanowires Seeded by Organic Monolayer-Coated Gold Nanocrystals, *J. Am. Chem. Soc.*, 2002, **124**(7), 1424–1429.

43 E. Mullane, H. Geaney and K. M. Ryan, Synthesis of silicon–germanium axial nanowire heterostructures in a solvent vapor growth system using indium and tin catalysts, *Phys. Chem. Chem. Phys.*, 2015, **17**(10), 6919–6924.

44 H. Geaney, C. Dickinson, W. Weng, C. J. Kiely, C. A. Barrett, R. D. Gunning and K. M. Ryan, Role of Defects and Growth Directions in the Formation of Periodically Twinned and Kinked Unseeded Germanium Nanowires, *Cryst. Growth Des.*, 2011, **11**(7), 3266–3272.

45 E. Mullane, T. Kennedy, H. Geaney, C. Dickinson and K. M. Ryan, Synthesis of Tin Catalyzed Silicon and Germanium Nanowires in a Solvent–Vapor System and Optimization of the Seed/Nanowire Interface for Dual Lithium Cycling, *Chem. Mater.*, 2013, **25**(9), 1816–1822.

46 N. Jeon, S. A. Dayeh and L. J. Lauhon, Origin of Polytype Formation in VLS-Grown Ge Nanowires through Defect Generation and Nanowire Kinking, *Nano Lett.*, 2013, **13**(8), 3947–3952.

47 Z. Su, C. Dickinson, Y. Wan, Z. Wang, Y. Wang, J. Sha and W. Zhou, Crystal growth of Si nanowires and formation of longitudinal planar defects, *CrystEngComm*, 2010, **12**(10), 2793–2798.

48 F. M. Davidson, D. C. Lee, D. D. Fanfair and B. A. Korgel, Lamellar Twinning in Semiconductor Nanowires, *J. Phys. Chem. C*, 2007, **111**(7), 2929–2935.

49 T. Hanrath and B. A. Korgel, Crystallography and Surface Faceting of Germanium Nanowires, *Small*, 2005, **1**(7), 717–721.

50 E. R. Hemesath, D. K. Schreiber, E. B. Gulsoy, C. F. Kisielowski, A. K. Petford-Long, P. W. Voorhees and L. J. Lauhon, Catalyst Incorporation at Defects during Nanowire Growth, *Nano Lett.*, 2012, **12**(1), 167–171.

51 Z. Yang, H. Chen, Y. Hou, F. Wu, J. Qiao, F. Pan, X. Lin and H. Bai, Effect of defective structure taking on the electronic and optical properties of InP nanowire, *Phys. B*, 2022, **640**, 414042.

52 S. Biswas, S. Barth and J. D. Holmes, Inducing imperfections in germanium nanowires, *Nano Res.*, 2017, **10**(5), 1510–1523.

53 S. Wang, Z. Shan and H. Huang, The Mechanical Properties of Nanowires, *Advanced Science*, 2017, **4**(4), 1600332.

54 J. Wang, X. Meng, X. Fan, W. Zhang, H. Zhang and C. Wang, Scalable Synthesis of Defect Abundant Si Nanorods for High-Performance Li-Ion Battery Anodes, *ACS Nano*, 2015, **9**(6), 6576–6586.

55 S.-H. Choi, G. Nam, S. Chae, D. Kim, N. Kim, W. S. Kim, J. Ma, J. Sung, S. M. Han, M. Ko, H.-W. Lee and J. Cho, Robust Pitch on Silicon Nanolayer–Embedded Graphite for Suppressing Undesirable Volume Expansion, *Adv. Energy Mater.*, 2019, **9**(4), 1803121.

56 J. Feng, Z. Zhang, L. Ci, W. Zhai, Q. Ai and S. Xiong, Chemical dealloying synthesis of porous silicon anchored by *in situ* generated graphene sheets as anode material for lithium-ion batteries, *J. Power Sources*, 2015, **287**, 177–183.

57 G. Schmuelling, N. Oehl, M. Knipper, J. Kolny-Olesiak, T. Plaggenborg, H.-W. Meyer, T. Placke, J. Parisi and M. Winter, Synthesis and electrochemical performance of surface-modified nano-sized core/shell tin particles for lithium ion batteries, *Nanotechnology*, 2014, **25**(35), 355401.

58 O. Riedel, A. Düttmann, S. Dühnen, J. Kolny-Olesiak, C. Gutsche, J. Parisi, M. Winter, M. Knipper and T. Placke, Surface-Modified Tin Nanoparticles and Their Electrochemical Performance in Lithium Ion Battery Cells, *ACS Appl. Nano Mater.*, 2019, **2**(6), 3577–3589.

59 D. Wang, C. Zhou, B. Cao, Y. Xu, D. Zhang, A. Li, J. Zhou, Z. Ma, X. Chen and H. Song, One-step synthesis of spherical Si/C composites with onion-like buffer structure as high-performance anodes for lithium-ion batteries, *Energy Storage Mater.*, 2020, **24**, 312–318.

60 W. Wang and P. N. Kumta, Nanostructured Hybrid Silicon/Carbon Nanotube Heterostructures: Reversible High-Capacity Lithium-Ion Anodes, *ACS Nano*, 2010, **4**(4), 2233–2241.

61 B. Luo, B. Wang, X. Li, Y. Jia, M. Liang and L. Zhi, Graphene-Confined Sn Nanosheets with Enhanced Lithium Storage Capability, *Adv. Mater.*, 2012, **24**(26), 3538–3543.
62 C. C. Nguyen and B. L. Lucht, Comparative Study of Fluoroethylene Carbonate and Vinylene Carbonate for Silicon Anodes in Lithium Ion Batteries, *J. Electrochem. Soc.*, 2014, **161**(12), A1933.
63 F. T. Huld, S. Y. Lai, W. M. Tucho, R. Batmaz, I. T. Jensen, S. Lu, O. E. Eleri, A. Y. Koposov, Z. Yu and F. Lou, Enabling Increased Delithiation Rates in Silicon-Based Anodes through Alloying with Phosphorus, *ChemistrySelect*, 2022, **7**(42), e202202857.
64 A. Garcia, S. Biswas, D. McNulty, A. Roy, S. Raha, S. Trabesinger, V. Nicolosi, A. Singha and J. D. Holmes, One-Step Grown Carbonaceous Germanium Nanowires and Their Application as Highly Efficient Lithium-Ion Battery Anodes, *ACS Appl. Energy Mater.*, 2022, **5**(2), 1922–1932.
65 K. Ogata, E. Salager, C. J. Kerr, A. E. Fraser, C. Ducati, A. J. Morris, S. Hofmann and C. P. Grey, Revealing lithium–silicide phase transformations in nano-structured silicon-based lithium ion batteries *via in situ* NMR spectroscopy, *Nat. Commun.*, 2014, **5**(1), 3217.
66 P. R. Abel, A. M. Chockla, Y.-M. Lin, V. C. Holmberg, J. T. Harris, B. A. Korgel, A. Heller and C. B. Mullins, Nanostructured $Si_{1-x}Ge_x$ for Tunable Thin Film Lithium-Ion Battery Anodes, *ACS Nano*, 2013, **7**(3), 2249–2257.
67 S. Abdul Ahad, S. Kilian, M. Zubair, V. A. Lebedev, K. McNamara, K. M. Ryan, T. Kennedy and H. Geaney, Amorphization driven Na-alloying in Si_xGe_{1-x} alloy nanowires for Na-ion batteries, *J. Mater. Chem. A*, 2021, **9**(36), 20626–20634.